LETTERS
PUBLISHED ONLINE: 13 NOVEMBER 2011 | DOI: 10.1038/NPHOTON.2011.270
nature photonics

On-chip optical isolation in monolithically integrated non-reciprocal optical resonators

Lei Bi[1]*, Juejun Hu[2], Peng Jiang[1], Dong Hun Kim[1], Gerald F. Dionne[1], Lionel C. Kimerling[1] and C. A. Ross[1]*

Non-reciprocal photonic devices, including optical isolators and circulators, are indispensible components in optical communication systems. However, the integration of such devices on semiconductor platforms has been challenging because of material incompatibilities between semiconductors and magneto-optical materials that necessitate wafer bonding, and because of the large footprint of isolator designs. Here, we report the first monolithically integrated magneto-optical isolator on silicon. Using a non-reciprocal optical resonator on an silicon-on-insulator substrate, we demonstrate unidirectional optical transmission with an isolation ratio up to 19.5 dB near the 1,550 nm telecommunication wavelength in a homogeneous external magnetic field. Our device has a small footprint that is 290 μm in length, significantly smaller than a conventional integrated optical isolator on a single crystal garnet substrate. This monolithically integrated non-reciprocal optical resonator may serve as a fundamental building block in a variety of ultracompact silicon photonic devices including optical isolators and circulators, enabling future low-cost, large-scale integration.

Non-reciprocal photonic devices that break the time-reversal symmetry of light propagation provide critical functionalities such as optical isolation and circulation in photonic systems. Although widely used in optical communications, such devices are still lacking in semiconductor integrated photonic systems[1,2] because of challenges in both materials integration and device design. On the materials side, magneto-optical garnets used in discrete non-reciprocal photonic devices show large lattice and thermal mismatch with semiconductor substrates, making it difficult to achieve monolithic integration of garnets with phase purity, high Faraday rotation and low transmission loss[3,4], and requiring wafer bonding to incorporate them on a semiconductor platform. On the device side, non-reciprocal mode conversion (NRMC) and non-reciprocal phase shift (NRPS) integrated optical isolators have large footprints with length scales from millimetres to centimetres[5,6], which severely limits the feasibility of large-scale and low-cost integration. Efforts have been pursued both in the monolithic integration of iron garnet and the exploration of other magneto-optical materials with better semiconductor compatibility. Polycrystalline $Y_3Fe_5O_{12}$ (YIG) films[3], epitaxial $Sr(Ti_{1-x}Fe_x)O_{3-\delta}$ (ref. 7), $Sr(Ti_{1-x}Co_x)O_{3-\delta}$ (ref. 8) and Fe-doped InP films[9] have been demonstrated to have promising magneto-optical performance at a wavelength of 1,550 nm. In relation to device design, several monolithic non-reciprocal photonic devices capitalizing on optical resonance effects (for example, magneto-optical photonic crystals[10], garnet thin-film based optical resonators[11], silicon ring resonators with magneto-optical polymer cladding[12] and modulated ring resonators using non-reciprocal photonic transitions[1]) have been theoretically analysed with a view to reducing the device footprint. However, the experimental realization of monolithic integrated devices on silicon has not been demonstrated so far due to material and fabrication difficulties. Currently, the only experimentally demonstrated optical isolators on silicon still rely on wafer bonding of Ce-doped yttrium iron garnet films grown on garnet single crystals to a silicon-on-insulator (SOI) Mach–Zehnder structure[13] or to an SOI ring resonator[14]. The hybrid integrated Mach–Zehnder device has a transverse-magnetic (TM) mode isolation ratio of 21 dB and insertion loss of ~8 dB (ref. 13) (with a device length of ~2 mm), and a very recently reported ring resonator has an isolation ratio of 9 dB and insertion loss of ~18 dB with a resonator diameter of 1.8 mm (ref. 14). Both devices featured non-uniform magnetic fields provided by bulk magnets. Compared to the hybrid solution, on-chip monolithic integration of non-reciprocal photonic devices offers high throughput, high yield, low cost and large scale, and thus has been sought for integrated photonic platforms for many years.

In this Letter, we report the first monolithically integrated optical isolator on an SOI platform. The device operates under a homogeneously applied magnetic field, and uses a design based on a patterned non-reciprocal optical resonator to significantly reduce the footprint[15]. This device combines three essential characteristics of an on-chip isolator: a monolithically integrated design, small footprint and good isolation performance. The device structure is shown in Fig. 1a. The isolator consists of a single-mode silicon racetrack resonator fabricated on an SOI wafer with a top cladding of 1-μm-thick SiO_2. Part of the SiO_2 top cladding is etched to form a 'window', which directly exposes the underlying silicon resonator waveguide surface. A magneto-optical film is subsequently deposited on the entire sample area without the need for etching. In this work, the film consisted of a polycrystalline garnet bilayer, $(Ce_1Y_2)Fe_5O_{12}$(80 nm)/$Y_3Fe_5O_{12}$(20 nm). By using a two-step deposition method (see Methods) with a thin YIG buffer layer, we successfully obtained phase-pure polycrystalline $(Ce_1Y_2)Fe_5O_{12}$ (Ce:YIG) films on silicon[16] (Supplementary Fig. S3) in which no crystalline material other than the garnet phase was present. The values of Faraday rotation for polycrystalline YIG and Ce:YIG films were $+100^\circ\ cm^{-1}$ and $-1{,}263^\circ\ cm^{-1}$, the saturation magnetizations were 130 e.m.u. cm^{-3} and 120 e.m.u. cm^{-3}, and the saturation fields were 100 Oe and 200 Oe, respectively. Because of the SiO_2 cladding, the optical mode interacts with the magneto-optical film only at the window region, where the silicon channel waveguide with garnet top-cladding layer provides strong NRPS of the TM-polarized mode due to the large index contrast between silicon (3.48) and magnetic garnets (~2.2) at ~1,550 nm (ref. 17).

Figure 1b shows a cross-sectional scanning electron microscopy (SEM) image of the fabricated device at the window section. When an in-plane homogeneous magnetic field is applied perpendicular to

[1]Department of Materials Science and Engineering, Massachusetts Institute of Technology, Cambridge, Massachusetts 02139, USA, [2]Department of Materials Science and Engineering, University of Delaware, Newark, Delaware 19716, USA. *e-mail: bilei@mit.edu; caross@mit.edu

© 2011 Macmillan Publishers Limited. All rights reserved.

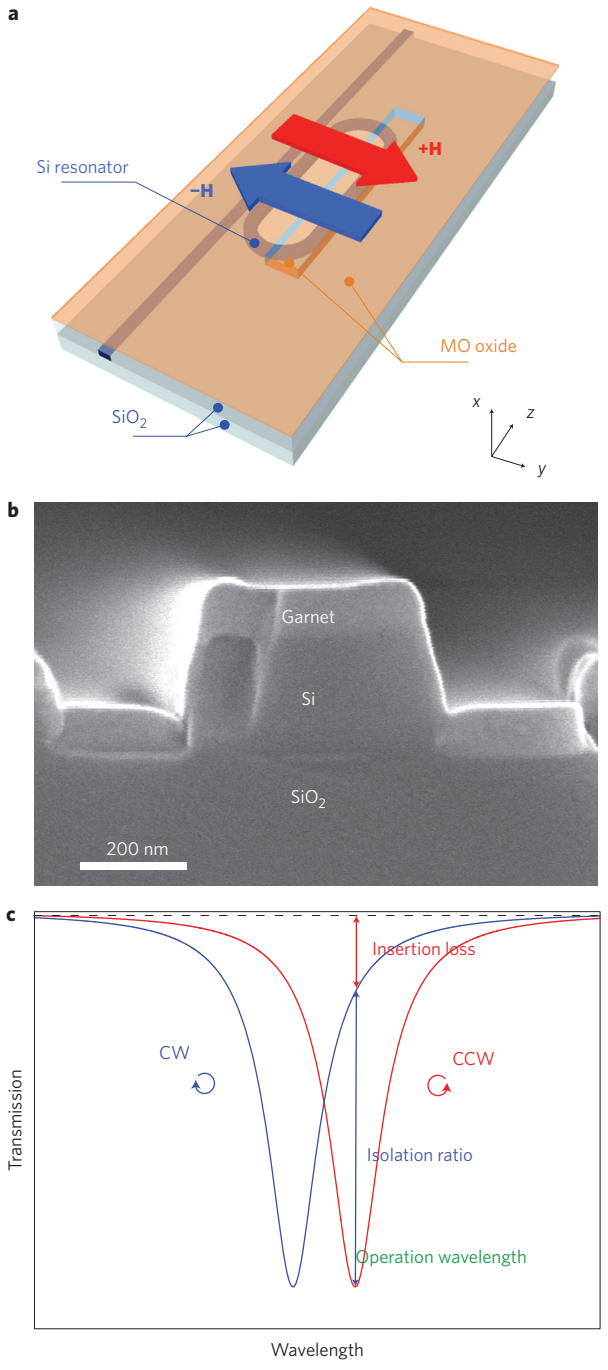

Figure 1 | Structure and operation principle of the monolithic non-reciprocal optical-resonator-based isolator. a, Schematic of the non-reciprocal optical resonator structure. **b**, Transverse cross-sectional SEM image at the window section of the resonator. A 100 nm garnet film layer (Ce:YIG(80 nm)/YIG(20 nm)) was deposited on the single-mode silicon channel waveguide. **c**, Operation principle for optical isolation. Maximum isolation ratio, corresponding insertion loss and operation wavelength range are shown.

the direction of light propagation, NRPS in the window section waveguide lifts the degeneracy of clockwise (CW) and counter-clockwise (CCW) resonant TM modes. Such non-degeneracy leads to non-reciprocal optical transmission in the wavelength range near the cavity resonance and thus achieves optical isolation. The operation principle is illustrated by the schematic TM-mode transmission spectra in Fig. 1c. The isolation ratio and corresponding excess insertion loss at CCW resonance are represented by the blue and red arrows, respectively. Unlike a conventional NRPS isolator using a Mach–Zehnder interferometer, the isolation ratio in this design cannot be compromised by power imbalance in the two waveguide arms of the Mach–Zehnder interferometer. A high isolation ratio can always be achieved in resonator-based devices as long as a high extinction ratio is achieved.

We measured the optical isolation performance of this device at near-infrared wavelengths by end-coupling light through the bus waveguide using tapered lens-tip fibres. A 1,500 Oe magnetic field was applied perpendicular to the direction of light propagation in the patterned resonator region across the whole sample using a permanent magnet. Instead of fixing the magnetic field and reversing the light propagation direction, we fixed the light propagation direction and reversed the magnetic field by reversing the poles of the permanent magnet to probe non-reciprocal resonance shift. These two processes are equivalent as they produce identical permittivity tensors in the magneto-optical material. The magnetic field orientation in our experiments was designed to induce NRPS for TM-polarized light due to a large H_y component asymmetry along the x-direction in the garnet film[2], and negligible NRPS for the transverse-electric (TE) mode. Transmission spectra for TM- and TE-polarized light near a wavelength of 1,550 nm are shown in Fig. 2a,b, respectively. The inset shows several adjacent resonance peaks. The TM-mode resonance peaks are observed to show a significant shift when reversing the direction of the applied magnetic field, whereas TE-mode resonant wavelengths remain almost unchanged, which is in excellent agreement with predictions. This is direct experimental evidence of optical non-reciprocity in our resonator structure. Using the definition in Fig. 1c, an isolation ratio up to 19.5 dB with a 10 dB isolation bandwidth of 1.6 GHz was achieved for the TM-polarized light at the 1,542 nm wavelength resonant peak. Compared to a typical linewidth of order 100 MHz in an infrared single-mode semiconductor laser[18,19], the device bandwidth is sufficient for optical isolation. The isolation bandwidth and isolation ratio can be further optimized by increasing the NRPS of the magneto-optical material and decreasing the insertion loss. The optical non-reciprocity of this device can be measured multiple times, as shown in Fig. 2c,d. To unequivocally assign the observed non-reciprocity to the magneto-optical NRPS effect, we repeated the measurements six times for both TM- and TE-polarized light, with the magnetic field direction reversed each time. The time interval between two measurements was ~30 s. A clear non-reciprocal resonant peak shift up to 18.2 ± 0.7 pm was observed for the TM-polarized light when the applied magnetic field switched polarity, which corresponds to a maximum isolation ratio of 19.5 ± 2.9 dB, whereas the non-reciprocal resonant peak shift of the TE-polarized light was only 3.5 ± 2.4 pm. A similar optical non-reciprocity with TM-mode resonance shift was also observed in another resonator device coated with a Bi:YIG/YIG polycrystalline thin film. A non-reciprocal TM-mode resonance shift of 14.8 ± 4.6 pm at 1,549.5 nm was observed, demonstrating that the device design is compatible with various magneto-optical materials. The optical resonance peak drift under the same applied field direction and between different measurements in both TM and TE modes is attributed to temperature fluctuations of the sample stage. With a thermal optical constant of $1.86 \times 10^{-4}\,K^{-1}$ for silicon, the temperature change of the resonator is calculated to be ~0.14 K during the measurements, yielding 22 pm resonance drift in both TM and TE modes. The insertion loss of our current device was 18.8 ± 1.1 dB, higher than the loss values of 15.6 dB (ref. 6) and 8–11 dB (ref. 5) reported in isolator devices made from epitaxial garnet films. This is attributed to loss resulting from the fabrication of the silicon resonator, rather than being inherent to the device design, and is analysed in the Supplementary Information.

© 2011 Macmillan Publishers Limited. All rights reserved.

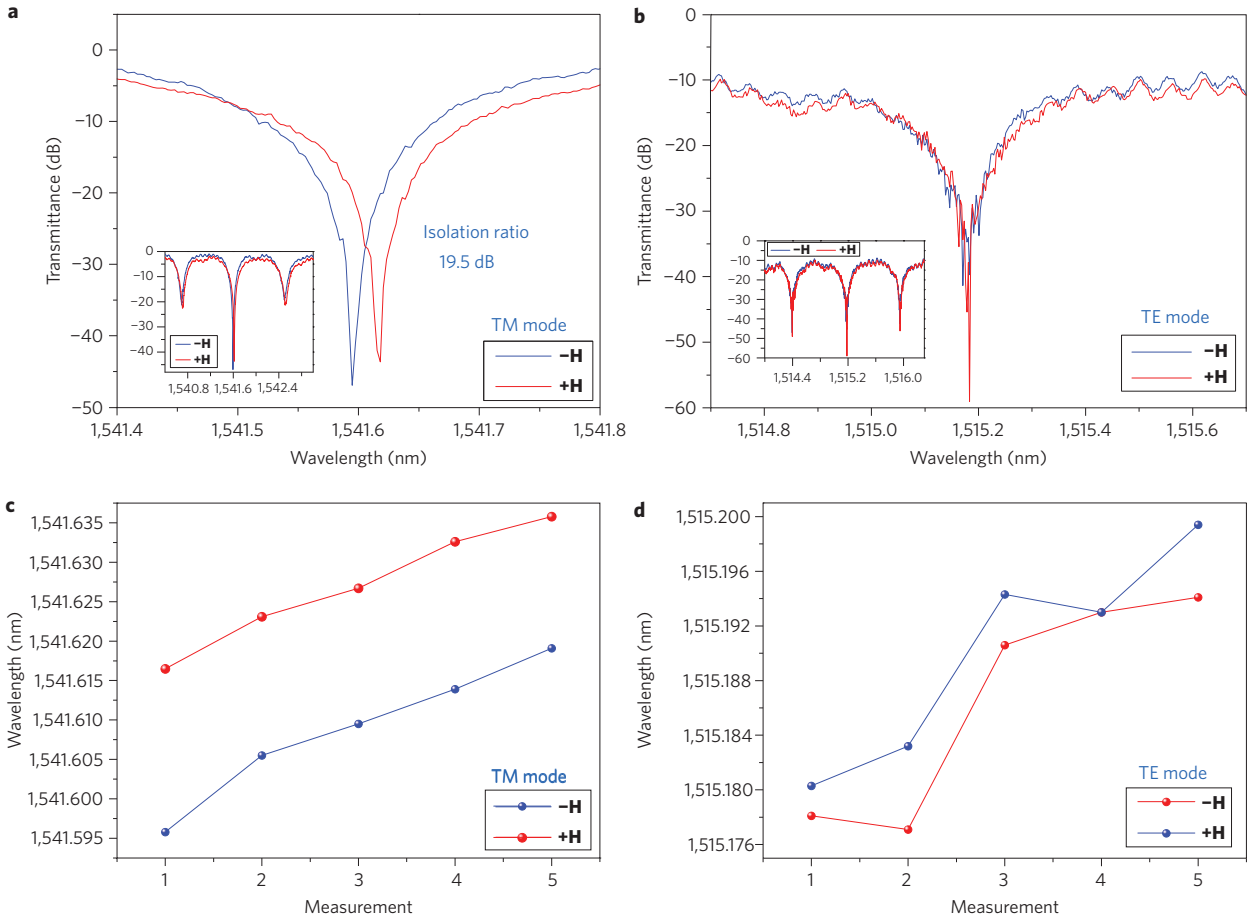

Figure 2 | Optical isolation performance of the isolator. a, TM-mode transmittance spectra under opposite applied magnetic field directions at near-critical coupling wavelengths. An isolation ratio up to 19.5 dB is achieved. **b**, TE-mode transmittance spectra under opposite applied magnetic field directions at near-critical coupling wavelengths. No obvious shift of the spectrum was observed. **c**,**d**, To test the reversibility and measurement error, the near-critical coupling resonance peak positions as a function of applied magnetic field directions were measured multiple times for the TM (**c**) and TE (**d**) modes. Peak shifts of 18.2±0.7 pm and 3.5±2.4 pm were observed for the TM and TE modes, respectively.

The isolation performance of this device can be derived analytically. As shown in Fig. 3, we define the length of the silicon resonator sections covered with SiO_2 and the magneto-optical cladding as L_0 and L_1 respectively. At critical coupling, the quality factor Q and free spectral range (FSR) of the resonator can be expressed as a function of the group indices of the L_0 and L_1 sections as[20]

$$Q = \frac{\pi(L_0 n_{g0} + L_1 n_{g1})}{\lambda_r \alpha L} \quad (1)$$

$$\mathrm{FSR} = \frac{\lambda_r^2}{L_0 n_{g0} + L_1 n_{g1}} \quad (2)$$

where $L = L_0 + L_1$ is the total cavity length, λ_r is the resonant wavelength, n_{g0} and n_{g1} are the group indices of the L_0 and L_1 sections, respectively (related to effective index by $n_g = n_{\mathrm{eff}} - (\delta n_{\mathrm{eff}}/\delta\lambda)\lambda$), and α is defined as the loss per unit length of the resonator, which is expressed by $\alpha = (\alpha_0 L_0 + \alpha_1 L_1 + 2\alpha_{\mathrm{junction}})/L$, with the three terms denoting the loss contributions from L_0 and L_1, and the junction loss between the two sections, respectively. The TM-mode resonance shift $\Delta\lambda$ can be written as

$$\Delta\lambda = \frac{\mathrm{FSR} \cdot L_1 \Delta\beta_{\mathrm{TM}}}{2\pi} \quad (3)$$

where $\Delta\beta_{\mathrm{TM}}$ is defined as the NRPS of TM-polarized light in the L_1 section, which describes the propagation constant difference between forward- and backward-propagating TM-mode polarized light at the critical coupling wavelength[2]. A detailed derivation can be found in the Supplementary Information. We define the device figure of merit as $F_{\mathrm{res}} = \Delta\lambda/w = (\Delta\lambda/\lambda_r)Q$, which describes the device performance by comparing the non-reciprocal resonance shift to the resonance peak width, where w is the full-width at half-maximum (FWHM) of the resonance peak. Using the expressions for Q and $\Delta\lambda$ above, the device figure of merit reduces to $F_{\mathrm{res}} = (L_1\Delta\beta_{\mathrm{TM}})/\alpha L$. When the loss of the magneto-optical waveguide section dominates, the figure of merit is further simplified as $F_{\mathrm{res}} = (L_1\Delta\beta_{\mathrm{TM}})/\alpha_1 L_1 = \Delta\beta_{\mathrm{TM}}/\alpha_1$, which is simply the figure of merit in terms of NRPS divided by optical loss per length of the magneto-optical waveguide. This result indicates that the ultimate performance of our design is limited only by the properties of the magneto-optical film and bus waveguide material. We have recently demonstrated a material loss of ~9 cm^{-1} in polycrystalline Ce:YIG/YIG and 5.3±0.8 dB cm^{-1} in As_2S_3/garnet waveguides[16], which predicts an insertion loss as low as 5–6 dB if fabrication is fully optimized (Supplementary Section IV).

To quantitatively evaluate device performance, we simulated the mode profile of the waveguide shown in the inset of Fig. 3 with the film mode matching (FMM) method using FIMMWAVE software[21].

© 2011 Macmillan Publishers Limited. All rights reserved.

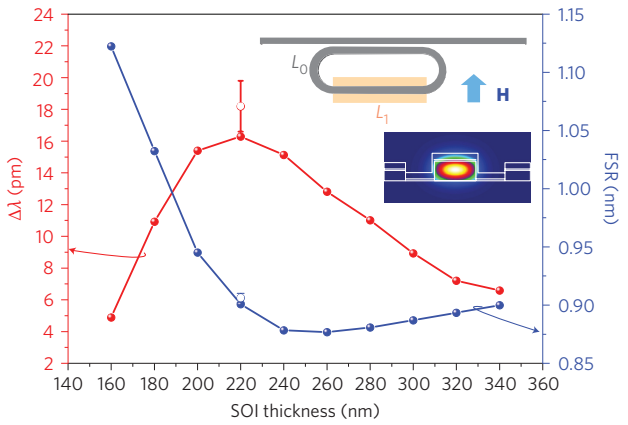

Figure 3 | Simulated device performance as a function of SOI waveguide height. Both non-reciprocal resonance shift and FSR were simulated as a function of SOI waveguide height. Inset: device layout and simulated TM mode profile using the experimentally observed waveguide cross-section of Fig. 1b, which were both used for resonance shift and FSR calculations. Experimental results are shown as open circles to compare with the simulation results.

The NRPS $\Delta\beta_{TM}$ per length of the waveguide was numerically simulated using the equation

$$\Delta\beta_{TM} = -\frac{2\beta_{TM}}{\omega\varepsilon_0 N}\iint \frac{K'' M_y}{n_0^4} H_y \partial_x H_y \mathrm{d}x\mathrm{d}y$$

(ref. 2) with a Faraday rotation value of $-1{,}263^\circ\ \mathrm{cm}^{-1}$ for polycrystalline Ce:YIG and $+100^\circ\ \mathrm{cm}^{-1}$ for YIG. β_{TM} is the TM-mode propagation constant, ω is the frequency, ε_0 is the vacuum dielectric constant, M_y is the magnetization of the magneto-optical material along the y-direction defined in Fig. 1, K'' is a material constant that relates the magnetization M_y to Faraday rotation Θ by $\Theta = -k_0 \frac{K'' M_y}{2n_0}$, n_0 is the isotropic refractive index of the magneto-optical material, k_0 is the vacuum wavenumber, and N is the power flow along the z-direction, defined by $N = \int\int (\mathbf{E} \times \mathbf{H}^* + \mathbf{E}^* \times \mathbf{H})_z \mathrm{d}x\mathrm{d}y$. In our analysis, the power flow along the z-direction is simulated using full vectorial expressions; that is, the electric field $\boldsymbol{E} = E_x\hat{x} + E_y\hat{y} + E_z\hat{z}$ and magnetic field $\boldsymbol{H} = H_x\hat{x} + H_y\hat{y} + H_z\hat{z}$ have non-trivial modal field components along the x-, y- and z-directions, where $\hat{x}$, $\hat{y}$ and $\hat{z}$ are the unit vectors along x, y and z directions respectively. Owing to the structural symmetry along the y-direction, the H_x field yields zero NRPS and does not contribute to the above equation. Using equations (2) and (3), we further simulated $\Delta\lambda$ and FSR as a function of the SOI waveguide thickness (Fig. 3). The FSR and $\Delta\lambda$ of our device were calculated to be 0.9016 nm and 15.9 pm, compared to measured values of 0.9009 nm and 18.2 pm at a wavelength of 1,542 nm (shown as open circles in the figure). The agreement is very good, with the difference in $\Delta\lambda$ possibly arising due to the use of a rectangular waveguide cross-section for the simulation and/or to a discrepancy between the simulated and experimental film thicknesses for the YIG and Ce:YIG layers.

Dispersion is another important factor for isolator devices. We measured the dispersion of the non-reciprocal phase shift $\Delta\lambda$ at several resonant wavelengths from 1,470 nm to 1,550 nm (Fig. 4). A weak dispersion of $\Delta\lambda$, varying from 21.7 ± 1.1 pm to 18.4 ± 0.7 pm, was observed with increasing wavelength. This behaviour results from two terms in equation (3): the positive dispersion of the FSR and the negative dispersion of the magneto-optical properties in Ce:YIG materials, decreasing the $\Delta\beta_{TM}$ term at longer wavelengths. The negative $\Delta\beta_{TM}$ dispersion is consistent with a previous materials study[22], and is attributed to a reduction in the oscillator strength for the $Ce^{3+}(4f)$–Fe^{3+}(tetrahedral) electronic transition at ~1–2 eV, which is considered to be the origin of the enhancement in the near-infrared magneto-optical effect in this material[23]. By incorporating Ce:YIG in the patterned resonator structure, the large negative dispersion of the magneto-optical properties is compensated by the positive dispersion of the FSR, resulting in the low dispersion seen in the device performance. Compared with conventional optical isolators, the advantage of the additional degree of freedom of dispersion control in our device is essentially achieved by using a strip-loaded waveguide structure and having both non-reciprocal and reciprocal sections in the resonator. Further fine-tuning of the dispersion of the group index in the reciprocal waveguide section with cladding materials may lead to devices with close-to-zero NRPS wavelength dependence.

From a device integration standpoint, the fact that magneto-optical non-reciprocal functionality has been demonstrated using low-optical-loss polycrystalline materials grown at a relatively low temperature is a significant step forwards for monolithic integration. This isolator design can be aligned to the laser output using the thermal optical effect so that the resonance wavelength coincides with the laser wavelength in the back-reflection direction. Alternatively, a drop port can be used on the ring resonator as the laser output. In this case the lasing wavelength is on-resonance, whereas the back-reflected light is off-resonance, and is rejected by the isolator, preventing back-coupling into the laser.

In conclusion, we have experimentally demonstrated the first monolithically integrated optical isolator on silicon with an isolation ratio up to 19.5 ± 2.9 dB for TM-polarized modes at 1,542 nm. Using a patterned silicon resonator coated with a magneto-optical garnet film, our device demonstrates the advantages of monolithic integration, ultracompact footprint, high isolation ratio, homogeneous magnetic field operation and controllable magneto-optical dispersion. This device architecture is compatible with a variety of magneto-optical materials that can be grown on the resonator. As a fundamental building block to achieve on-chip optical non-reciprocity, this device may be used in a range of monolithically integrated photonic devices on silicon, including optical

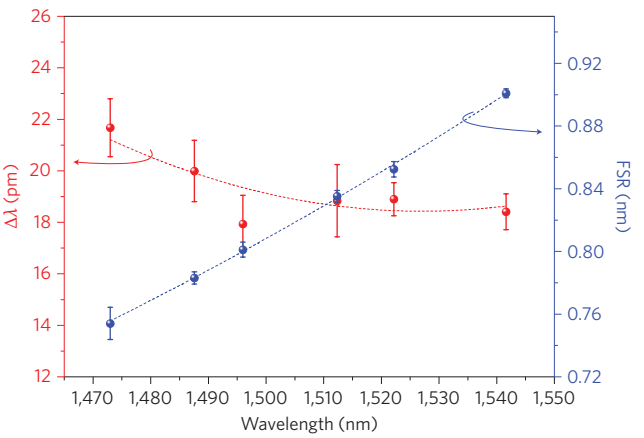

Figure 4 | Dispersion relations of the resonance peak shift and FSR of the optical isolator. Dashed lines are guides to the eye. Experimentally measured resonance peak shift and FSR show opposite dispersion relations, which is due to the dispersion relation of the magneto-optical effect in the Ce:YIG material. The patterned resonator structure may therefore provide dispersion control of device performance by controlling the FSR dispersion of the resonator structure. Error bars indicate the standard deviation of measurements.

© 2011 Macmillan Publishers Limited. All rights reserved.

isolators and circulators, therefore enabling wafer-scale integration of non-reciprocal devices for future silicon photonic systems.

Methods

Material and device fabrication. The fabrication process flow for the non-reciprocal racetrack resonator on an SOI substrate is shown in Supplementary Fig. S1. A bare silicon racetrack resonator was first fabricated on a Si(220 nm)/SiO_2(3 μm)/Si SOI wafer (SOI Tech.). A hydrogen silsesquioxane (HSQ) resist (Dow Corning XR-1541 4%) was spin-coated on the wafer to a thickness of 60 nm. HSQ patterns (width, 450 nm) were defined by electron-beam exposure and development in a tetramethylammonium hydroxide developer. The silicon channel waveguides and resonators were formed by reactive ion etching (RIE) in HBr gas. The mask HSQ layer on silicon was removed by etching the samples in a 100:1 HF solution for 2 min. The radius of the ring region of the racetrack was 45 μm and the length of the straight region was 200 μm. The gap between the resonator and the bus waveguide was 200 nm. A 1-μm-thick flowable oxide (Fox-25, Dow Corning) was spin-coated on the resonator and rapid thermal annealed at 1,050 °C for 1 min to form a SiO_2 top-cladding layer[24]. Optical lithography was then carried out on a mask aligner (OAI) to define the window region on the racetrack resonator using NR9-1000PY photoresist (Futurrex). An RIE step was carried out using CHF_3 to etch the SiO_2 layer by 600 nm in the window region, followed by an HF (100:1) etch process to obtain a smooth silicon waveguide surface. After the HF etch, atomic force microscopy measurements were carried out to confirm that the silicon resonator surface had been exposed, followed by an ultrasonic cleaning process in isopropanol. The devices were then transferred to a pulsed laser deposition (PLD) chamber for magneto-optical thin film deposition[16]. A KrF pulsed laser operating at a wavelength of 248 nm with a fluence of 2–3 J cm^{-2} was used for the deposition. Bi:YIG or Ce:YIG films were deposited on the device using a two-step deposition method, in which a 20-nm-thick $Y_3Fe_5O_{12}$ film was first deposited by PLD at 550 °C with an oxygen partial pressure of 10 mtorr and subsequently annealed at 850 °C for 5 min under nitrogen flow to crystallize, then an 80-nm-thick $Ce_1Y_2Fe_5O_{12}$ or $Bi_{1.8}Y_{1.2}Fe_5O_{12}$ film was deposited at 650 °C on the YIG buffer layer with an oxygen partial pressure of 5 mtorr. The presence of garnet phases was confirmed by X-ray diffraction analysis.

Optical transmission and isolation characterization. Waveguide and resonator transmission and isolation measurements were performed on a Newport AutoAlign workstation in combination with a HP/Agilent tunable laser (Supplementary Fig. S2). The transmitted optical signal was analysed using an optical vector analyser (LUNA Technologies). The samples were cleaved to form end facets and placed on a thermostat stage kept at 25 °C. Tapered lens-tip fibres were used to couple light from the laser into and out of the device through the end facets. Reproducible coupling was achieved using an automatic alignment system with a spatial resolution of 50 nm. By scanning the input wavelength, transmission spectra in the wavelength range 1,470–1,560 nm were collected. NRPS measurements for the resonator devices were also carried out on the same stage. A permanent magnet was placed close to the device with the magnetic field direction perpendicular to the light wave vector. The magnetic field across the sample was ~1,500 Oe. By reversing the magnetic field direction, device non-reciprocity was measured and calculated from the transmission spectra.

Received 15 June 2011; accepted 28 September 2011; published online 13 November 2011

References

1. Yu, Z. & Fan, S. Complete optical isolation created by indirect interband photonic transitions. *Nature Photon.* **3,** 91–94 (2009).
2. Dötsch, H. *et al.* Applications of magneto-optical waveguides in integrated optics: review. *J. Opt. Soc. Am. B* **22,** 240–253 (2005).
3. Sung, S., Qi, X. & Stadler B. J. H. Integrating yttrium iron garnet onto nongarnet substrates with faster deposition rates and high reliability. *Appl. Phys. Lett.* **87,** 121111 (2005).
4. Boudiar, T. *et al.* Magneto-optical properties of yttrium iron garnet (YIG) thin films elaborated by radio frequency sputtering. *J. Magn. Magn. Mater.* **284,** 77–85 (2004).
5. Shintaku, T. Integrated optical isolator based on efficient nonreciprocal radiation mode conversion. *Appl. Phys. Lett.* **73,** 1946–1948 (1998).
6. Fujita, J., Levy, M., Osgood, R. M. Jr, Wilkens, L. & Dötsch, H. Waveguide optical isolator based on Mach–Zehnder interferometer. *Appl. Phys. Lett.* **76,** 2158–2160 (2000).
7. Kim, H. S., Bi, L., Dionne, G. F. & Ross, C. A. Magnetic and magneto-optical properties of Fe-doped $SrTiO_3$ films. *Appl. Phys. Lett.* **93,** 092506 (2008).
8. Bi, L., Kim, H. S., Dionne, G. F. & Ross, C. A. Structure, magnetic properties and magnetoelastic anisotropy in epitaxial $Sr(Ti_{1-x}Co_x)O_3$ films. *New J. Phys.* **12,** 043044 (2010).
9. Zaman, T. R., Guo, X. & Ram, R. J. Semiconductor waveguide isolators. *J. Lightwave Technol.* **26,** 291–301 (2008).
10. Wang, Z. & Fan, S. Optical circulators in two-dimensional magneto-optical photonic crystals. *Opt. Lett.* **30,** 1989–1991 (2005).
11. Kono, N., Kakihara, K., Saitoh, K. & Koshiba, M. Nonreciprocal microresonators for the miniaturization of optical waveguide isolators. *Opt. Express* **15,** 7737–7751 (2007).
12. Jalas, D., Petrov, A., Krause, M., Hampe, J. & Eich, M. Resonance splitting in gyrotropic ring resonators. *Opt. Lett.* **35,** 3438–3440 (2010).
13. Shoji, Y., Mizumoto, T., Yokoi, H., Hsieh, I. & Osgood, R. M. Magneto-optical isolator with silicon waveguides fabricated by direct bonding. *Appl. Phys. Lett.* **92,** 071117 (2008).
14. Tien, M., Mizumoto, T., Pintus, P., Kromer, H. & Bowers, J. E. Silicon ring isolators with bonded nonreciprocal magneto-optical garnets. *Opt. Express* **19,** 11740–11745 (2011)
15. Bi, L. *Magneto-Optical Oxide Thin Films and Integrated Nonreciprocal Photonic Devices.* PhD thesis, Massachusetts Institute of Technology (2011).
16. Bi, L., Hu, J., Dionne, G. F., Kimerling, L. & Ross, C. A. Monolithic integration of chalcogenide glass/iron garnet waveguides and resonators for on-chip nonreciprocal photonic devices. *Proc. SPIE* **7941,** 794105 (2011).
17. Espinola, R. L., Izuhara, T., Tsai, M., Osgood, R. M. & Dötsch, H. Magneto-optical nonreciprocal phase shift in garnet/silicon-on-insulator waveguides. *Opt. Lett.* **29,** 941–943 (2004).
18. Duan, G. H., Favre, H. & Le Guen, D. FM noise and linewidth reduction in a 1.5 μm InGaAsP DFB laser coupled to an external fiber resonator. *Opt. Commun.* **15,** 111–114 (1988).
19. Henry, C. H. Theory of the linewidth of semiconductor lasers. *IEEE J. Quantum Electron.* **18,** 259–264 (1982).
20. Hu, J. *Planar Chalcogenide Glass Materials and Devices.* PhD thesis, Massachusetts Institute of Technology (2009).
21. Integrated Optics Software FIMMWAVE 4.5, Photon Design, Oxford, UK; available at http://www.photond.com
22. Higuchi, S., Furukawa, Y., Tekekawa, S., Kamada, O. & Kitamura K. Magneto-optical properties of cerium-substituted yttrium iron garnet single crystals grown by traveling solvent floating zone method. *Jpn J. Appl. Phys.* **38,** 4122–4126 (1999).
23. Gomi, M., Furuyama, H. & Abe, M. Strong magneto-optical enhancement in highly Ce-substituted iron garnet films prepared by sputtering. *J. Appl. Phys.* **70,** 7065–7067 (1991).
24. Holzwarth, C. W., Barwicz, T. & Smith, H. I. Optimization of hydrogen silsesquioxane for photonic applications. *J. Vac. Sci. Technol. B* **25,** 2658–2661 (2007).

Acknowledgements

The authors thank Jie Sun for discussions on silicon resonator fabrication. The support of the National Science Foundation and an Intel Fellowship for Lei Bi is gratefully acknowledged.

Author contributions

L.B. conducted the theoretical simulation, material fabrication, device fabrication and testing. J.H. conceived the device and contributed to theoretical simulation and device testing. P.J. and D.H.K. contributed to material fabrication. G.F.D., L.C.K. and C.A.R. supervised and coordinated the project. All authors contributed to writing the paper.

Additional information

The authors declare no competing financial interests. Supplementary information accompanies this paper at www.nature.com/naturephotonics. Reprints and permission information is available online at http://www.nature.com/reprints. Correspondence and requests for materials should be addressed to L.B. and C.A.R.

© 2011 Macmillan Publishers Limited. All rights reserved.